DMIP retreat 2006-2007 schedule

April 27, 2007

8:00-8:30 Breakfast
8:30-8:35 Opening remarks—Katsuyuki Taguchi
8:35-9:55 Session 1 (80 min)—Yong Du

Overview of Rotating slant-hole SPECT project— Benjamin M. W. Tsui
- Completeness conditions in rotating multi-segment variable slant angle SPECT technique—Jingyan Xu

Overview of Dosimetry project—Eric C. Frey
- The impact of VOI definition on activity estimation accuracy in quantitative SPECT and planar imaging methods—Bin He

"Overview of ultrasound research in DMIP" and "Ultrasound Elasticity Image Guidance for External Beam Partial Breast Irradiation"—Emad M. Boctor and Hassan Rivaz

9:55-10:10 Break

10:10-11:45 Session 2 (90 min)—Martin J. Stumpf

Overview of Gated cardiac SPECT project—Benjamin M. W. Tsui
- The Development and Application of Simultaneous Cardiac and Respiratory Gated ECT/CT Dataset from the 4D NCAT Phantom—Taek-Soo Lee
- Three-D cardiac motion estimation: study on cost function and initial estimates—Jing Tang

Overview of x-ray CT project—Katsuyuki Taguchi
- Image-Based "Reconstruction" for Motion Compensated Cardiac CT—Zhihui Sun

Patient dose measurements during cardiac CT Angiography procedures—Mahesh Mahadevappa

11:45-13:15 Lunch

13:15-14:30 Session 3 (75 min)—Jingyan Xu

Overview of Dual isotope SPECT project—Eric C. Frey
- Optimization of Tc injected activity in simultaneous dual-isotope myocardial perfusion SPECT imaging using a three-class channelized Hotelling observer study—Xiaolan Wang
- Efficient Monte Carlo based scatter estimation for SPECT imaging with photon track reuse—Yong Du

Overview of SPECT/MRI and Prostate cancer projects—Benjamin M. W. Tsui
- Performance Evaluation of Block-Iterative Algorithms for SPECT Reconstruction—Chi Liu

14:30-15:40 Guided poster sessions (70 min)—Yuchuan Wang, Jing Tang, and Katsuyuki Taguchi
- Measurement of Glucose Uptake in the Contused Spinal Cord of Adult Rats Using small animal PET imaging—Jianhua Yu
- A simulation platform for SPECT-MRI system—Si Chen
- Prostate Cancer and Prostate Monoclonal Antibody Imaging (Prostascint^{TM})—Susanne Hemker
- Mutual Information Based Multimodality registration for Cumulated Activity Distribution Estimation—Na Song
- Development of "SmileyZ" Phantom for Evaluating the Accuracy of Material Decomposition—Mengxi Zhang
- A Robust Meshing and Calibration Approach for Sensorless Freehand 3D Ultrasound—Hassan Rivaz

15:40-15:50 Break

15:50-16:55 Session 4 (65 min)—Bin He

Overview of Animal imaging project—Benjamin M. W. Tsui
- High-Resolution Small Animal SPECT/CT Imaging of Atherosclerotic Plaques in ApoE-/- Mice Using Tc-99m Annexin-V and Contrast Enhanced CT—Greta S. P. Mok
- Physical phantom evaluation of the efficiency of reconstruction and compensation methods on quantitative SPECT prostate imaging—Alex K. F. Kwok

Progress on 3 dimensional bone geometry assessments in vivo—Thomas J. Beck

16:55-17:10 Award selection
17:10-17:20 Award presentation
17:20-17:25 Closing remarks—Benjamin M. W. Tsui

TITLE:
Performance Evaluation of Block-Iterative Algorithms for SPECT Reconstruction

AUTHORS:
Chi Liu, Lana Volokh, Xide Zhao, Jingyan Xu, Taek-Soo Lee, and Benjamin M.W. Tsui

PURPOSE:
The purpose of this study is to evaluate the performance of four block-iterative algorithms, ordered-subsets expectation-maximization (OS-EM), rescaled block-iterative EM (RBI-EM), modified row-action maximum likelihood algorithm (RAMLA) and rescaled block-iterative maximum *a posteriori* EM (RBI-MAP-EM), for In-111 ProstaScint® SPECT image reconstruction.

METHODS AND MATERIALS:
The 3D NCAT phantom with realistic In-111 ProstaScint® activity distribution was used in the study. Noise-free and noisy projections of the phantom obtained using a medium-energy general-purpose (MEGP) collimator were generated using Monte Carlo simulation methods. For each algorithm, the projection data were reconstructed with the compensations for attenuation, collimator-detector response and scatter. Image quality was evaluated in terms of FWHM of a profile through a small blood vessel, normalized mean square error (NMSE), ensemble normalized standard deviation (NSD_E) of a uniform region of interest (ROI) in the reconstructed image measured from 30 noise realizations, and regional NSD (NSD_R) of an ROI measure from 1 noise realization.

RESULTS:
The results indicated that, RBI-EM has superior performance than that of OS-EM when less than 4 views per subset were used and similar performance when 4 or more views per subset were used. Modified RAMLA provides similar image quality with a slower convergence rate than that of OS-EM. Using well-chosen parameters, RBI-MAP-EM provides increased noise smoothing with less loss in resolution and error.

CONCLUSIONS:
We conclude that when compared with OS-EM and RBI-EM and modified RAMLA have the same performance at a slower convergence rate, while the RBI-MAP-EM has superior performance and can potentially improve image quality.

FUNDING SOURCES:
This work is supported by a DOD Idea Development Award #DAMD17-02-1-0112 and a research contract from the General Electric HealthCare.

TITLE: Completeness conditions in rotating multi-segment variable slant angle SPECT technique

AUTHORS: Jingyan Xu, Chi Liu, and Benjamin M. W. Tsui

PURPOSE:

The objective is to investigate the completeness condition for SPECT image reconstruction using a rotating multi-segment variable slant angle (RMSVSH) collimator.

METHODS AND MATERIALS: Each segment on a RMSVSH collimator consists of collimator holes with slant angle that increases from the edge of the collimator (outer slant angle) to the center (inner slant angle), therefore forms a 1D divergent beam geometry with a focal line behind and parallel to the collimator surface resulting in an enlarged common-volume-of-view compared to the RMSSH collimator with slanted parallel holes. From a single camera position with 360º collimator rotation, the Radon space resembles a distorted torus with a spindle shaped unsampled core. It is necessary to have multiple camera positions in RMSVSH SPECT so that the sampled and unsampled regions from different camera positions complement each other to fill the whole Radon space. We performed simulations to confirm the data completeness condition. We designed two phantoms consisting of stacked disks oriented so as to detect any data insufficiency in RMSVSH SPECT acquisition. The simulated RMSVSH collimator has a diameter of 40 cm, the inner slant angle 45º, and the outer slant angle 30º. We simulated noise-free RMSVSH projection from 1, 2, and 3 camera positions, the angular separation between the camera positions is 60º. Reconstructed images were obtained using the ML-EM algorithm for RMSVSH SPECT at 100^{th} iteration.

RESULTS: The acquisition parameters determined that 3 camera positions would satisfy the data completeness condition. For the first phantom, reconstructed images from 1 camera position showed strong blurring artifacts, but no obvious difference between using 2 and 3 camera positions. For the second phantom which was designed to detect the data insufficiency using 2 positions only, the reconstructed images using 1 and 2 camera positions both showed strong blurring artifacts, but visually artifacts-free using data from all 3 positions.

CONCLUSIONS: We investigated the completeness condition for RMSVSH SPECT technique. Our simulations support the analysis. This study provides guidelines for determining the RMSVSH SPECT data acquisition geometry so that fully 3D reconstruction is possible.

FUNDING SOURCES: NIH R01 EB 001983

TITLE:
The impact of VOI definition on activity estimation accuracy in quantitative SPECT and planar imaging methods

AUTHORS:
Bin He and Eric C. Frey

PURPOSE:
Accurate estimation of organ activity is an essential part of patient-specific dosimetry. We have previously compared several quantitative imaging methods in terms of accuracy and precision of activity estimation using experimental and simulated phantoms. However the accuracy and precision also depend on the accuracy of definition of volumes of interest (VOIs). The goal of this work was thus to study the impact of VOI definition on activity estimation accuracy.

METHODS AND MATERIALS:
In this work we performed Monte Carlo simulation (MCS) studies using shifted and randomly perturbed VOIs to assess the impact on activity estimation accuracy on quantitative SPECT (QSPECT), and planar (QPlanar) methods. The realistic NCAT phantom was used with organ activities that model ^{111}In ibritumomab tiuxetan. Projection data were obtained using MCS that realistically model the image formation process including interactions in the collimator-detector system. In the mis-registration study, VOIs were sub-pixel shifted by distances ranging from -1 to 1 pixel in both transaxial directions. In the mis-definition study, VOIs of the liver and left kidney were first manually defined to exactly contain organs. Each control point defining the VOI was then randomly perturbed to one of the nearest or next-nearest neighbor pixels in three ways: random directions (Random), outward (Dilation), and inward (Erosion). The estimates from modified VOIs were compared to those from non-modified VOIs and average errors were computed.

RESULTS:
Up to one pixel mis-registration or mis-definition resulted in up to 8% error in organ activity estimates, with the largest errors for small or low-uptake organs. For mis-registration, errors were linear in the shift for both the QSPECT and QPlanar methods. QPlanar was less sensitive to perturbations than QSPECT, especially for dilation and erosion mis-definition.

CONCLUSIONS:
Mis-registration and mis-definition had a larger impact on activity estimates for small and low uptake organs. Mis-registration generally had larger effects than mis-definition. The different imaging methods evaluated responded differently to the errors from mis-registration and mis-definition. Thus, sensitivity to VOI definition errors should be an important criterion in evaluating quantitative imaging methods.

FUNDING SOURCES:
NIH R01, "Quantitative SPECT for Targeted Radionuclide Therapy"

Emad M. Boctor, Ph.D.

There has been an increasing interest in minimally invasive US-guided interventions that require precise placement of a surgical tool (needle, tissue ablator, etc.) to the anatomical target. To address this problem, I have developed a collection of novel technologies and integrated those in prototype systems.

I introduce multiple system embodiments that involve robotics, tracking, anatomical modeling, ultrasound image processing, and elasticity monitoring. The underlying themes in these systems are (1) simultaneous tracking of surgical tool with respect to the US images and (2) monitoring physiological changes, specifically tissue coagulation, throughout the procedure.

My main contribution to the first theme is inventing a robust method for 2D and 3D ultrasound probe calibration with a closed-form solution. As a result, one can discern the unknown spatial transformation between image pixels and tracker coordinates in real-time, in-vivo while the patient is being scanned. I also introduced a novel methodology for in-vivo quality control of tracked US systems, by capturing system errors that manifest in changes of calibration parameters. The concept, mathematical formulation, and experimental evaluation are presented and demonstrated in-vitro experiments.

With respect to the second theme, I presented a rapid US-based approach to monitor ablative therapy by optimizing shape parameters. My method involves the integration of a biomechanical computational model of the tissue, a correlation approach to estimate and track tissue deformation, and an optimization method to solve the inverse problem of recovering the shape parameters in the volume of interest. I demonstrate convergence and reliability on simulated data and present successful monitoring of tissue ablation of ex-vivo bovine liver samples.

TITLE:

The Development and Application of Simultaneous Cardiac and Respiratory Gated ECT/CT Dataset from the 4D NCAT Phantom

AUTHORS:

Lee, Taek-Soo; Shilov, Mikhail; Tsui, Benjamin

PURPOSE:

We developed and evaluated the applications of simultaneous cardiac and respiratory gated SPECT/CT and PET/CT datasets derived from the 4D NCAT phantom.

METHODS AND MATERIALS:

To create useful SPECT, PET and CT datasets that include the simultaneous cardiac and respiratory motions, we generated 3D NURBS-based Cardiac-Torso (NCAT) phantoms at different gated time frames. The respiratory motion of the body excluding the heart was modeled by a total of 24 separate 3D NCAT phantoms over a respiratory cycle, and the beating heart was simulated separately with 48 frames over a cardiac cycle for each of the 24 respiratory phases. There were then combined to generate simulated Tc-99m sestamibi myocardial perfusion (MP) SPECT projections with different gating schemes and relative phases. Noise free SPECT projections were generated using an analytical projector, and grouped into different gating schemes including no gating, 6 respiratory-gates with 8 cardiac-gates, and various combinations of them. Each projection was reconstructed using the 3D OS-EM without any correction and with attenuation corrections using different attenuation maps: an average over the entire cardiac or respiratory cycle, a map at the end-inspiration phase, and a map at the corresponding respiratory phase to simulate those obtained from different radionuclide-based or x-ray based CT system. The image artifacts of the reconstructed images were compared by visual inspection of the polar maps.

RESULTS:

The gated MP SPECT images from the study demonstrate that respiratory motion generated a signature artifactual decrease in both the anterior and inferior regions of the MP polar map whose magnitude increases with the amplitude of the respiratory motion. While gating the SPECT data reduced artifacts, these artifacts were further reduced when the attenuation map was also gated.

CONCLUSIONS:

We conclude that the 4D NCAT phantom set that allows modeling of simultaneous cardiac and respiratory motions offers a useful and important tool the study of the effects of cardiac and respiratory motions, gating schemes and correction methods in MP SPECT/CT and PET/CT.

FUNDING SOURCES:

R01 EB 000168
R01 HL068075

TITLE:
Three-D cardiac motion estimation: study on cost function and initial estimates

AUTHORS:
Jing Tang, W. Paul Segars, and Benjamin M.W. Tsui

PURPOSE:
The 3D cardiac motion estimation technique we previously developed generates different results in estimating the motion vector field (MVF) from NCAT phantom heart images when modified (to cover non-heart voxels) NCAT built-in MVF or zero MVF is used as the initial estimate. The goal of this research is to study the convergence of the motion estimation algorithm through investigating on the cost function and the initial estimates applied, and therefore explain the above mentioned difference.

METHODS AND MATERIALS:
The cost function in our 3D cardiac motion estimation algorithm consists of two terms, one is an image matching error term and the other is a weighted strain energy term. When the modified NCAT MVF serves as the initial estimate, it sustains so that the resulted MVF are close to the NCAT MVF in all radial, circumferential, and longitudinal directions. This means that the strain energy constraint does not suppress the NCAT MVF in any direction. When zero initialization is applied, the resulted MVF contains little circumferential and longitudinal components and its radial component is noticeably different from the radial motion in the NCAT MVF. We assume that difference exists between resulted MVFs with the two different initial estimates only because the former result contains tangential motion that can not be detected from given images with zero initialization. The following investigations have been performed. To prove that the edge-orthogonal motion field converges to the same value, we test on an initial estimate being the unit value of the intensity change in the gradient direction. To prove that suppressing tangential motion will result in the same estimated MVF when either modified NCAT or zero MVF is applied as the initial estimate, we add a term to the original cost function of the motion estimation algorithm. This term is the weighted squared norm of the cross product of the MVF and the gradient of the image.

RESULTS:
With the unit edge-orthogonal motion field as an initial estimate, the resulted MVF is similar to the MVF estimated with zero initialization. When using the cost function with an extra term added for suppressing tangential motion, we obtain similar results from modified NCAT MVF initial estimate and from zero initialization. The extra term in the cost function does not affect the resulted MVF when zero initialization is applied.

CONCLUSIONS:
The energy constraint in our 3D cardiac motion estimation algorithm does not suppress tangential motion that can not be detected from intensity images. The difference between the estimated motion fields from the modified NCAT MVF estimate and the zero initialization is merely because the former one contains tangential components while the latter one does not. The cost function with the extra term aiming to minimize the tangential motion seems to have a global minimum.

FUNDING SOURCES:
NIH R01 EB 000168 & R01 HL068075

TITLE:
Image-Based "Reconstruction" for Motion Compensated Cardiac CT

AUTHORS:
Zhihui Sun, W. Paul Segars, Elliot K. Fishman, Benjamin M.W. Tsui, and Katsuyuki Taguchi

PURPOSE:
In cardiac CT images, motion artifacts produced by heart motion are much severer at rapidly moving phases than at slowly moving phases. We can significantly reduce motion artifacts in the images at rapidly moving phases by generating those images using image at a quasi-stationary phase. The goal of this work was to develop a method to transform a reference image at a chosen quasi-stationary phase to motion-artifact reduced target images at arbitrary cardiac phases, using given 2D motion vectors—the given vectors were defined on spatially sparse nodes in the reference image and specified the motions from the reference phase toward several temporally sparse phases.

METHODS AND MATERIALS:
We first worked on the given motion vectors to locate the starting point in the reference image for each pixel in the target image, and then calculated the grayscale values for the off-grid starting points in the reference image and applied those values to the target image. Since the given motion vectors were only defined on a finite set of time frames, the motion vectors toward an image at arbitrary time of interest were obtained by temporally interpolating given motion vectors using cubic B-splines. The temporally interpolated motion vectors remained "push" vectors which were defined on the sparse nodes of the reference image. The next step was to find the starting point in the reference image that corresponds to each pixel in the target image. We converted those "push" vectors to "pull" vectors which were defined on the sparse points of the target image, and spatially interpolated sparse "pull" vectors using quickhull algorithm to get dense "pull" vector for every pixel of the target image. The located starting points in the reference image were off-grid, hence their grayscale values were obtained by applying bilinear interpolation to adjacent pixels of the reference image. The final warped image was generated by applying the pixel value of corresponding starting point in the reference image to each pixel in the target image.

RESULTS:
We evaluated the warping method using the true images and true motion vectors generated by 4D NCAT phantom. A warped image together with the reference image and target image is shown in figure 1. The reference image is at a quasi-stationary phase, and the target image is at an arbitrary rapidly moving phase. Comparing the warped image (Figure 1(c)) with true reference image (Figure 1(a)) and true target image (Figure 1(b)), we can see that the warped image is generally consistent with the true target image and presents as little motion artifact as reference image does. However, some artifacts (Figure 1(c), arrows) indicate the warping (transformation) does not produce sufficient results, which may be caused by improper interpolation or the lack of third components of 3D vectors or both.

CONCLUSIONS:
We have developed and implemented the method to generate images at arbitrary cardiac phases by using the cardiac image at quasi-stationary phase and time dependent motion vectors. The method reduces the motion artifact of the images at rapidly moving phases. However, there remain problems such as insufficient warping. We will solve those problems in the further study.

FUNDING SOURCES:
American Heart Association Beginning Grant-In-Aid 0665431U,
NIH R01 EB001838
Start-up fund of the Division of Medical Imaging Physics

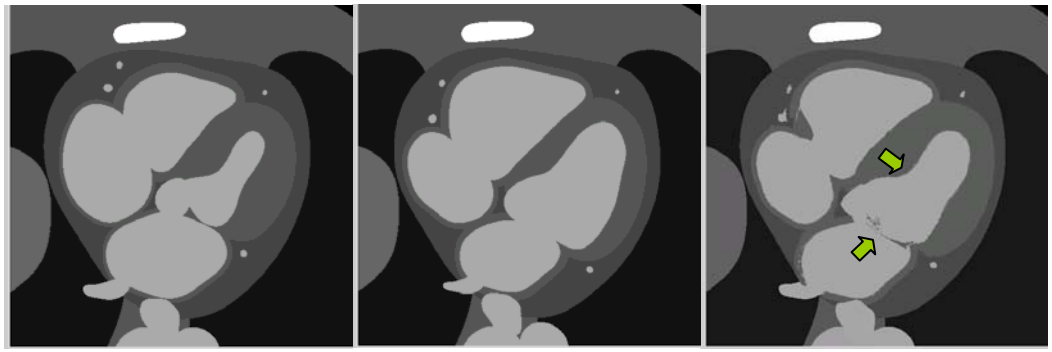

(a) (b) (c)

Figure 1 (a) true reference image. (b) true target image. (c) warped target image

Thomas J. Beck, Sc. D.

Progress on 3 dimensional bone geometry assessments in vivo

The strength of human bones changes through life and is altered in certain diseases so that fractures become more likely. The effects are totally without symptoms so that disease is often discovered after fractures occur. Most strength changes in bone are in the dimensional geometry, i.e., the dimensions that determine internal stresses under loading forces. A reliable method for detecting weakened bones would permit application of available, effective treatments. The two dimensional method developed at Johns Hopkins for measuring the geometric properties of the hip from a 2-dimensional DXA scan is widely used in clinical research and has been licensed by a scanner manufacturer for incorporation into their software. Because of the 2-dimensional nature of DXA images and the fact that scan protocols were not optimized to measure geometry, the method is imprecise, subject to systematic errors and requires some assumptions that do not always hold. To address these problems a 3-dimensional method is under development using a limited number of dual energy x-ray projections. The goal is to derive sufficient geometric information for a 3-dimensional engineering simulation of loading under both physiologic and traumatic conditions. The initial work is intended to be used to evaluate the femur where the most serious fractures occur and will employ a commercial DXA scanner with multiple projection capability. I will provide an overview of the research in its current status beginning with a description of the approach, the underlying principles and technical hurdles we have yet to overcome. Pending the availability of IRB approval, some data on human subjects will be shown together with the analysis approach to be used in the engineering simulation.

TITLE:
Optimization of Tc injected activity in simultaneous dual-isotope myocardial perfusion SPECT imaging using a three-class channelized Hotelling observer study

AUTHORS:
Xiaolan Wang, Xin He and Eric C. Frey

PURPOSE:
Crosstalk in simultaneous dual isotope (Tc-99m/Tl-201) myocardial perfusion SPECT (MPS) results in reduced image quality. One way to reduce the crosstalk to the Tl data is to reduce the injected activity (IA) of the Tc-99m agent. However, this will increase the noise in the Tc image. The image quality must thus be judged with respect to the 3-class nature of the task that is done with rest/stress imaging, i.e., classifying the patient as normal or having fixed or reversible defects. We have previously developed methodology for performing and analyzing 3-class observer studies and in this work applied them to investigate the optimal Tc-99m IA.

METHODS AND MATERIALS:
Projection data were generated using Monte Carlo simulations of a population of 24 NCAT phantoms that models patient variations in gender, organ and body size, heart orientation, organ uptake, and defect size, contrast, and position. Three Tc IAs were studied: 8, 16, and 24 mCi, while one Tl IA of 3 mCi was modeled. The projection data sets for each IA included equal numbers from each defect class. We investigated 2 strategies: separate acquisition (no crosstalk) and simultaneous acquisition with ideal crosstalk compensation using the true noise-free crosstalk. All reconstructions were performed using OS-EM with compensation for attenuation, detector response, and scatter. Reconstructed Tc and Tl images were post-filtered with a 3D Butterworth filter and reoriented to short-axis images. These were analyzed in a 3-class channelized Hotelling observer study to produce a volume under a 3-class ROC surface (VUS). For each strategy and IA level, the optimal combination of uptakes and filter cutoff frequency of those studied was the one giving the highest VUS.

RESULTS:
We found that 24 mCi injected activity gave the highest VUS for separate acquisition while 16 mCi gave the highest VUS for simultaneous acquisition.

CONCLUSIONS:
This study demonstrates that there is an optimal injected activity for dual isotope simultaneous acquisition studies. It also demonstrates the applicability of 3-class ROC analysis methods in finding the optimal parameters for myocardial perfusion imaging.

FUNDING SOURCES:
This study is supported by NIH grant R01-EB000288.

TITLE:

Efficient Monte Carlo based scatter estimation for SPECT imaging with photon track reuse

AUTHORS:

Yong Du, Martin J. Stumpf, and Eric C. Frey

PURPOSE:

Scatter estimation using Monte Carlo (MC) simulation is more accurate than analytical and model-based methods, especially for non-uniform objects and large scatter orders. However, use of MC in reconstruction-based compensation is still limited by computation time. A powerful method for improving computation time is convolution-based forced detection (CFD). In CFD, MC simulation is used to track photons to form an effective scatter source (ESS). The ESS is then attenuated, convolved plane-by-plane with the DRF, and projected. One way to improve the speed is to reuse the ESS for multiple projection views. However, this can reduce the accuracy of the estimated projections. We have developed a new MC scatter estimation (MCSE) method that can efficiently estimate scatter in each projection view without a loss in accuracy.

METHODS AND MATERIALS:

In our MCSE, MC simulation of photon tracks in the object and analysis of the tracks to estimate the ESS are performed separately. The MC simulated photon tracks are saved in a photon list in memory. For each iteration or subset, the same photon list is used to compute the ESS, taking into account changes in the activity estimate by adjusting initial weights of each photon. Thus, the MC photon tracking is only required once during the whole reconstruction. We validated the MCSE method by comparing its scatter estimates in both photopeak and downscatter energy windows in uniform and nonuniform attenuators to those from a SimSET MC simulation and an analytic scatter model (ESSE).

RESULTS:

Our MCSE method performed similarly to SimSET for photopeak and downscatter windows in both uniform and nonuniform attenuators. The scatter estimates were similar in accuracy to ESSE for uniform objects and a photopeak energy window, but more accurate in other cases. The time to generate and reanalyze the list are about equal, indicating that photon track reuse results in a savings of almost 50% when a large number of ESSs are estimated. The time to generate a low noise projection using our MCSE is faster than SimSET by a factor of more than 3000.

CONCLUSIONS:

We have developed a fast efficient MC scatter estimation method that reuses photon tracks to accurately estimate scatter for SPECT imaging. The method can be used with iterative reconstruction techniques to compensate for scatter and downscatter.

FUNDING SOURCES:

Funded by the Public Health Service Grant R01 CA 109234 and NIBIB Grant R01 EB000288

TITLE:

Measurement of Glucose Uptake in the Contused Spinal Cord of Adult Rats Using small animal PET imaging

AUTHORS:
Jianhua Yu, Rishi D.S. Nandoe, Jurgen Seidel, Martin Oudega, Benjamin Tsui and Martin Pomper

PURPOSE:
The purpose of this work is to study the glucose metabolism changes after moderate contusion injury in the adult rats, and to longitudinally quantify the glucose uptake levels in the injured regions using small animal PET imaging techniques.

METHODS AND MATERIALS:
We contused the ninth thoracic vertebra (T9) of the adult rats moderately using Infinite Horizon impactor (IH; impact force = 225 kDyne). A total of 5 injured rats and 2 control rats were injected with ^{18}F-FDG and scanned sequentially under the VISTA PET system and the CT subunit of Gamma Medica XSPECT/CT system. Six 0.4~0.6mm diameter beads soaked with ^{18}F-FDG were taped separately on the rats to guide the PET/CT image co-registration. Best-fit line scatter correction (SC) and CT-based attenuation correction (AC) were performed on the PET data. After co-registration, three region-of-interests (ROIs) with 2mm diameter were determined along the transaxial slice on the T8-9, T5-6 and T11-12 regions using the CT images. The pixel intensity values were measured in the same ROIs on the PET images, and further corrected for partial volume and spillover effects by computing the recovery coefficient (RC) in the Monte Carlo simulation. Based on the corrected pixel values, injected radioactivity and body weight, we computed the standardized uptake values (SUV) for each segment of spine to analyze the glucose uptake in the spinal cord at different time points, and to compare those of the different injured levels with the controls.

RESULTS:
The recovery coefficient for partial volume and spillover effects was 1.36 based on the Monte Carlo simulations results. Using this coefficient, we found that the average SUVs for the glucose uptake in the T8-9 level at 1.5hour, 3days, 7days, and 21days after contusion injury were 1.53±0.04, 1.58±0.13, 1.50±0.17 and 1.34±0.20 respectively, which were 8.12%, 11.59%, 5.79% and -5.56% higher than those of the controls. In addition, the SUVs for ROIs located at T8-9 level at these time points were 11.31%, 14.36%, 29.49% and 40.64% higher than those at T5-6 level, and 23.17%, 39.42%, 32.96% and 36.44% higher compared with those at T11-12 level.

CONCLUSIONS:
We observed and quantified the glucose uptake at the injured site increased in the first two weeks, and then gradually went down to the normal level. Compared with the uninjured part of the spinal cord, the contused position showed 10% ~ 40% higher glucose uptake. This study shows that *in vivo* small animal PET imaging provides a powerful tool for quantitative assessment of the glucose metabolic rates in the spinal cord of rats.

FUNDING SOURCES:
This work was supported by grant 017.001.265 from the Netherlands Organization and grant CA092781 from NIH.

TITLE:
A simulation platform for SPECT-MRI system

AUTHORS:
Si Chen

PURPOSE:
To build up a simulation platform for the SPECT-MRI system under investigation.

METHODS AND MATERIALS:
GATE is proposed for Monte-Carlo simulation for pinhole or multi-pinhole based SPECT system. Scintillation detectors are well modeled in GATE. In this study, we proposed to build up a module to simulate the CdZnTe detector response of incident Gamma photons. Hole trapping effect and other effects on the electron-hole pair collection are modeled based on semi-conductor physics. The pulse formation of pre-amplifier circuits will also be considered. This module will be used to process the list-mode output of Gamma photon simulation in GATE to generate the detector output of the whole Monte-Carlo simulation.

Object-Oriented Development interface for NMR (ODIN) is proposed for MRI simulation. ODIN is a free open source C++ software framework to develop, simulate and run magnetic resonance sequences on different platforms. It can be used for simulating the spin-physics of the sequence (Bloch-Torrey equations) using a virtual phantom to generate a virtual MR signal. System imperfections (eddy currents, B1 inhomogeneity, noise) can be switched on/off at will during the simulation. We will study how to input the NCAT phantom to the ODIN for MRI simulation.

The interaction of the SPECT and MRI system will also be considered in the simulation. The high magnetic field of MRI system and the electric field and heat generated by RF coil may affect the CdZnTe detector properties and the analog part of circuits. The SPECT system, which will be inserted in the MRI system, may also have some impact on the inhomogeneity of the magnetic field. These effects of physics will be mathematically modeled and synchronized between the two simulation system by using time stamp of list mode data in GATE and pulse sequence in ODIN.

RESULTS:
Some work has been done on the GATE modeling. The MRI part is still under investigation

CONCLUSIONS:
Hopefully we will build up this platform which can simulate and predict the behavior of futural real SPECT-MRI system with reasonable accuracy.

FUNDING SOURCES:

TITLE: Prostate Cancer and Prostate Monoclonal Antibody Imaging (Prostascint™)

AUTHORS: Susanne Hemker and B.M.W. Tsui

PURPOSE: The objective of this review is to explain the biological background of prostate cancer and monoclonal antibody imaging using In-111-capromab pendetide.

Prostascint Imaging: Indium In-111 Capromad Pendetide (ProstaScint™) is a conjugate containing a murine antibody directed against a glycoprotein expressed by the prostate epithelium (Prostate Specific Membrane Antigen, PSMA). Expression of the prostate-specific antigen (PSA) is higher in prostate carcinoma cells than in normal prostate tissue and higher in metastasis than in primary tumors. Although a rising PSA level is indicative of recurrent or residual disease, it is not specific to disease location. ProstaScint has been primarily used for patients with a clinical suspicion of recurrent or residual prostate cancer. ProstaScint detects lymph node metastatsis but although it may localize bone metastasis, radionuclide bone scans show a much higher sensitivity in the evaluation of skeletal involvement. Because PSMA is found on benign and malignant prostate epithelial cells, ProstaScint can not be used for prostate cancer screening.

In a phase I trial, Wynant *et al*.[1] tested capromab in 40 patients with metastatic prostate cancer imaged on bone and/or CT scans. Of these, 38 patients had positive bone scans, and six had soft-tissue disease visible on CT scans. Among the patients with positive bone scans, Wynant *et al*. found that only 5 of the 38 (13%) had all of their lesions detected, while 17 of the 38 (45%) had no evidence of disease, according to scans conducted using capromab. Capromab successfully imaged four of the six patients (66%) with soft-tissue disease.

In a clinical study[2] of 152 patients with newly diagnosed prostate cancer, sensitivity and specificity of a ProstaScint scan in detecting pelvic lymph node metastases were 62% and 72% respectively.

The other clinical setting explored was that of distinguishing local versus systemic extent of disease in patients experiencing a PSA relapse after radical prostatectomy. This is an important clinical setting, as approximately 30% of patients develop PSA relapse following prostatectomy. Several studies looked at post-prostatectomy patients with rising PSA. ProstaScint imaging was capable of detecting recurrent prostate cancer at low PSA levels. However, in a study of 42 patients [3] only 7 of 15 men (46.7%) with ProstaScint uptake isolated to the prostatic fossa showed a durable response to salvage radiation therapy. The authors conclude that based on these findings patients might be better treated based on the rate of increase in PSA rather than on routine scanning with this test.

In an effort to improve the interpretability and value of capromab imaging, there has been interest in fusing capromab-obtained images with anatomic images derived from CT or MRI[5]. DeWyngaert *et al*.[4] described the technical approach to such image corregistration. Schettino *et al*. [6] performed ordinary capromab scans of 58 patients, who then had their capromab images fused with CT or MRI and reread. There was a significant difference between the readings of capromab-only and capromab-fusion scans, implying a high false-positive rate for capromab-only scans. False positive results occur most often in areas of nonspecific uptake. Blood vessels can also make scan interpretation difficult.

References:

1 Wynant GE *et al*. (1991) Immunoscintigraphy of prostatic cancer: preliminary results with ^{111}In-labeled monoclonal antibody 7E11-C5.3 (CYT-356). Prostate 18: 229–241

2 Manyak MJ *et al*. (1999) Immunoscintigraphy with indium-111-capromab pendetide: evaluation before definitive therapy in patients with prostate cancer. Urology 54: 1058–1063

3 Wilkinson S, Chodak G. The role of 111indium-capromab pendetide imaging for assessing biochemical failure after radical prostatectomy. J Urol. 2004 Jul;172(1):133-6.

4 DeWyngaert JK (2004) *et al*. Procedure for unmasking localization information from ProstaScint scans for prostate radiation therapy treatment planning. Int J Radiat Oncl Biol Phys 60: 654–662

5 Sodee,D.B.; Sodee,A.E.; Bakale,G Synergistic value of single-photon emission computed tomography/computed tomography fusion to radioimmunoscintigraphic imaging of prostate cancer. Semin.Nucl.Med., 2007, 37, 1, 17-28

6 Schettino CJ *et al*. (2004) Impact of fusion of indium-111 capromab pendetide volume data sets with those from MRI or CT in patients with recurrent prostate cancer. Am J Roentgenol 183: 519–524

TITLE:
Describing Three-class Task Performance: Three-class Linear Discriminant Analysis and Three-class ROC Analysis

AUTHORS:
Xin He and Eric C. Frey

PURPOSE:
Binary ROC analysis has solid decision-theoretic foundations and a close relationship to linear discriminant analysis (LDA). In particular, for the case of Gaussian equal covariance input data, the area under the ROC curve (AUC) value has a direct relationship to the Hotelling trace. Many attempts have been made to extend binary classification methods to multi-class. For example, Fukunaga extended binary LDA to obtain multi-class LDA, which uses the multi-class Hotelling trace as a figure-of-merit, and we have previously developed a three-class ROC analysis method. This work explores the relationship between conventional multi-class LDA and three-class ROC analysis.

METHODS AND MATERIALS:
First, we developed a linear observer, the three-class Hotelling observer (3-HO). For Gaussian equal covariance data, the 3-HO provides equivalent performance to the three-class ideal observer and, under less strict conditions, maximizes the signal to noise ratios for classification of all pairs of the three classes simultaneously. The 3-HO templates are not the eigenvectors obtained from multi-class LDA. Second, we show that the three-class Hotelling trace, which is the figure-of-merit in the conventional three-class extension of LDA, has significant limitations. Third, we demonstrate that, under certain conditions, there is a linear relationship between the eigenvectors obtained from multi-class LDA and 3-HO templates.

RESULTS and CONCLUSION:
We conclude that the 3-HO based on decision theory has advantages both in its decision theoretic background and in the usefulness of its figure-of-merit. Additionally, there exists the possibility of interpreting the two linear features extracted by the conventional extension of LDA from a decision theoretic point of view.

FUNDING SOURCES:
This work was supported by the National Institutes of Health under Grants R01-EB000288 and R01-HL068575.

TITLE: **Mutual Information Based Multimodality registration for Cumulated Activity Distribution Estimation**

AUTHORS:
Na Song and Eric C. Frey

PURPOSE:
In treatment planning of targeted radionuclide therapy (TRT) for cancer it is desirable to give patients a radiation dose that is high enough to kill tumors but not too high to avoid causing adverse effects in normal organs. However, to date, there has only been weak evidence of a dose-response TRT, making predictions of response or adverse effects difficult. One possible explanation is that non-uniform distribution of the therapeutic agent inside tumors or normal organs, resulting in non-uniform dose-distributions. Voxel-based dosimetry methods could provide a better prediction of a dose-response relationship. These methods require as an input a 3D map of the cumulated activity, i.e., the integral of the time-activity curve (TAC). Reconstruction methods have been developed that would allow estimation of this 3D cumulated activity distribution based on SPECT imaging performed at multiple time points. While implementing this method, the position of the patient and the internal organs and tumors will be different during different SPECT imaging sessions. In the mean time, noise in the SPECT images will result in non-uniformities in the reconstructed images and make it difficult to obtain accurate and precise estimation of the cumulated activity in voxels. To overcome this obstacle, we need to implement image registration at first. The purpose of this work is to register image datasets of different modalities at different time points so that more accurate organ definition and cumulated activity estimation can be achieved.

METHODS AND MATERIALS:
Mutual information-based image registration methods begin with the estimation of the joint probability of the intensities of corresponding voxels in the two images. These methods differ in terms of the comparative ease of matching intensity images across modalities and the ability to discard intensity patterns in each modality that is not relevant to registration. Mutual information based image registration methods and direction set (Powell's) searching method are used to register image datasets. It includes registration between SPECT and CT datasets (3D to 3D different modality) obtained at different time points to aid in organ definition, registration amongst SPECT datasets (3D to 3D same modality) obtained at different time points to allow pixel-by-pixel estimation of cumulated activity, registration between planar images and projections of CT images (2D to 3D different modality) to provide thickness maps for geometric mean compensation of planar images and registration between SPECT or CT images with planar images (2D to 3D) for quantitative planar processing methods.

RESULTS:
Mutual information based registration is an effective method to register images between different modalities. We obtained reasonable registration results in most cases. However, for the registration between SPECT or CT images and planar images, good results can not be obtained in XZ angle and YZ angle directions because of the lackness of angle sensitivity. So the misregistration effects caused by these two angle directions to cumulated activity have to be further reviewed. After applying registration results generated in mutual information based registration methods to the ROI, the effects to cumulated activity can be reviewed with quantitative planar method.

CONCLUSIONS:
In order to improve the accuracy of cumulated activity estimation, registration is an important factor to be concerned. Mutual information based registration methods are adopted for its effectiveness in multi modality registration. We believe it will provide significant improvement to the accuracy of cumulated activity development.

FUNDING SOURCES: This work is funded by Public Health Service Grant R01-CA109234.

TITLE:
Development of "SmileyZ" Phantom for Evaluating the Accuracy of Material Decomposition

AUTHORS:
Mengxi Zhang and Katsuyuki Taguchi

PURPOSE:
The idea of material decomposition with x-ray CT imaging has been enthusiastically studied in 1980s, since people believed that it is useful in reducing noise dependency and patient dose. Recently developed photon-counting x-ray detector (PCXD) allows us to require data from adjacent multiple energy bins, thus, has revitalized our passion toward material decomposition. The problem, however, is the lack of good phantoms to evaluate the accuracy of material decomposition. Therefore, the purposes of this study are (1) to design a "SimleyZ" phantom for material decomposition and (2) to assess its usefulness.

METHODS AND MATERIALS:
Four key aspects for designing the phantom are (1) materials, (2) shapes, (3) locations, (4) sizes. Among all these four, the choice of materials is considered to be the most important. Guidelines for defining the materials are to categorize them into three major types: bony materials with high attenuation coefficient, soft-tissue type materials with low attenuation coefficient, and a third material with K-edge effect. The choice of this third material is proven to be crucial in the estimation accuracy. Considering ultimate contrast and clinical practice, we used dry spine, dense blood (1.25 of normal density), adipose and iodine-water (1.25% iodine by weight) as final materials. Shapes in this phantom are all cylinders, considering the convenience of calculating projection intersection. Sizes can be customized with respect to different CT scanners (micro-CT and human CT, for instance). We evaluated the usefulness of "SmileyZ" phantom in image domain material decomposition. The choices of basis functions are "BW" (referring to bone, water), and "BWI" (referring to bone, water and iodine), respectively. Data acquisitions include multi-energy bin using PCXD, mono-energy with PCXD, and Dual Kvp intensity integration. Cone-beam weighted ramp filtering is applied for image reconstruction. We then evaluated the accuracy of material decomposition in terms of effective Z map, synthesized image and decomposed coefficient map.

RESULTS:
The definition of "SmileyZ" phantom is shown below. "Eyeballs" consist of iodine-water (smaller circle) and spine (bigger circle). The accuracy of material decomposition is shown by the synthesized image at 32keV and 35keV. The original reconstructed image (figure 3) and the synthesized image based on BWI decomposition both show "close-open eyes" effects, while synthesized image based on BW decomposition has no such effects. This clearly demonstrates the accuracy of material decomposition in one aspect.

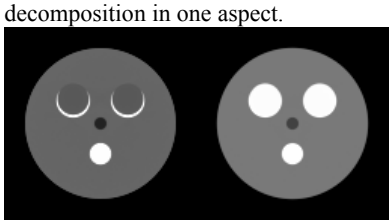

32KeV 35KeV
Figure1, BWI, 5-bin

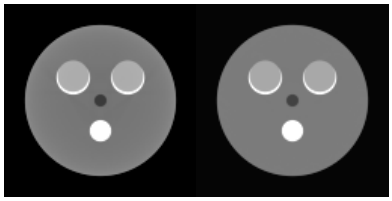

32KeV 35KeV
Figure2, BW, 5-bin

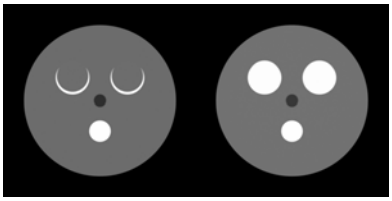

32KeV 35KeV
Figure3, Reconstructed

CONCLUSIONS:
The phantom is developed and the accuracy of material decomposition is evaluated. The evaluation results show the utility of "SmileyZ" phantom. Future works include precision study and extending "SmileyZ" phantom to allow ellipsis shape objects. Based on the phantom, we will further develop the decomposition algorithm to improve accuracy and extend to human computed tomography research.

FUNDING SOURCES:
DMIP start-up funds.

TITLE:
High-Resolution Small Animal SPECT/CT Imaging of Atherosclerotic Plaques in ApoE-/- Mice Using Tc-99m Annexin-V and Contrast Enhanced CT

AUTHORS:
G.S.P. Mok, B.M.W. Tsui, , J. Yu, Y. Wang, A. Tsao, D. Bedja, J. Yu, K. Gabrielson, S. Nimmagadda, F. Bengel and M.G. Pomper.

PURPOSE:
Atherosclerotic plaques are the major cause of coronary artery diseases and stroke. The objective of this study is to evaluate the application of high-resolution small animal SPECT/CT for longitudinal plaque imaging especially in the differentiation of stable and unstable lesions in ApoE-/- mice using ^{99m}Tc Annexin-V and contrast enhanced CT techniques.

METHODS AND MATERIALS:
Previously we developed high-resolution single and multi-pinhole SPECT techniques for small animal imaging including instrumentation, accurate system calibrations, 3D image reconstruction and compensation methods for improved image quality. The methods were applied in longitudinal studies to investigate the development and characteristics of atherosclerotic plaques in a series of ApoE-/- mice that were fed with fatty diet. Pairs of ApoE-/- and control mice were imaged with 2-3 weeks interval using a Gamma Medica-Idea dual-head SPECT/CT system that were fitted with 1mm single pinhole or new multi-pinhole collimators starting at age 18-week . The animals were injected with ~4-7 mCi of ^{99m}Tc labeled Annexin-V which targets apoptotic cells clustered mostly in unstable lesions. For better correlation of the activity distribution with anatomy, Venestra VC was administered to the animals before CT scans to improve soft tissue contrast and visualization of the blood vessels. To further confirm the focal uptake with plaques, we imaged the aorta region where plaques first appeared with high-resolution ultrasound, and performed autoradiography and histology study in the same aorta area.

RESULTS:
Focal ^{99m}Tc Annexin V uptakes were found in the ApoE-/- mice starting at age 18-week. Contrast enhanced CT images allow better correlation of the focal uptakes with anatomy indicating initial growth of plaques in the aorta region. Correlation of focal uptakes with plaques is confirmed with ultrasound, autoradiography and histology images. In a longitudinal study of an animal, we found an initial increase in activity concentration in a focal uptake followed by a decrease possibly indicating the growth and stabilization phases of plaque development.

CONCLUSIONS:
We conclude that molecular imaging in ApoE-/- mice using high-resolution SPECT/CT techniques with ^{99m}Tc Annexin-V and contrast enhanced CT provides great potentials in understanding the development and characteristics of atherosclerotic plaques. Future works include further correlating SPECT/CT images with images from other imaging modalities such as PET & MRI for better characterization of plaque vulnerability.

FUNDING SOURCES:
This work is supported by the NIH research grant EB001558

TITLE:

Physical phantom evaluation of the efficiency of reconstruction and compensation methods on quantitative SPECT prostate imaging

AUTHORS:

Alex K.F. Kwok[1], Yuchuan Wang[1], Yong Du[1], Benjamin M.W. Tsui[1], Martin Pomper[1]

1. Dept of Radiology, Johns Hopkins Medical Institute, USA

PURPOSE:

The objective of this project was to evaluate the quantitative accuracy of SPECT using physical phantoms and the GE Hawkeye Millennium^{TM} VG dual detector SPECT/CT system. Particular interest derives from SPECT imaging of prostate cancer, in which target radioactivity is complicated by that in surrounding tissue and bladder.

METHODS AND MATERIALS:

Experimental SPECT/CT phantom studies are performed to investigate the effect of size, radioactivity level and partial volume on the accuracy of quantitation. The phantoms were designed to mimic activity distributions found in prostate SPECT imaging. The SPECT projections acquired were reconstructed with filtered back projection (FBP), with ordered subset-expectation maximization (OSEM) without and with attenuation correction and additional collimator-detector response (CDR) and scatter compensation, and with additional correction for partial volume effect (PVE). Calibration factor in terms of voxel intensity/μCi was determined using a point source with known radioactivity. Estimated radioactivity from phantom sources was determined from the SPECT reconstructed images, using calibration factor and intensity sum over volume-of-interests (VOIs) with boundaries determined by CT image. Quantitative accuracy of the different image reconstruction and compensation methods was determined from the estimated and known radioactivity within the phantoms.

RESULTS:

The results demonstrated that quantitative accuracy progressively improved from FBP (70%) to OS-EM with compensations (up to ~5%) in cases not complicated by PVE. In cases where PVE became important, the quantitative accuracy decreased depending on the relative size and activity concentration of adjacent sources. Correction of PVE improves the quantitative accuracy approaching those from isolated sources, and a tendency has shown that stronger sources are less susceptible to PVE under the correction scheme. In experiments designed in analogy with prostate SPECT imaging where the size and activity concentration of the tumor are relatively small compared to the closely adjacent bladder, OSEM with all compensations with an appropriate update number significantly increases the quantitative accuracy within the tumor volume by 50% or more as compared to conventional FBP. Quantitative SPECT image reconstruction with compensation for image degrading factors substantially improves SPECT quantitation accuracy. This is particularly relevant to prostate SPECT where the size and activity concentration of the tumor are small compared to the closely adjacent bladder.

Qualitative evaluation

Experiment investigating PVC – noticeable difference between SPECT reconstructed with FBP and OSEM with compensations

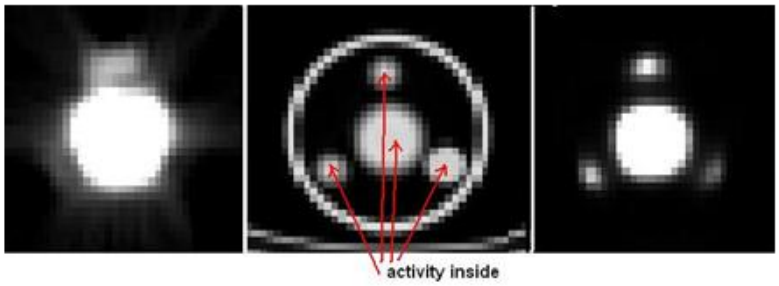

SPECT
Filtered backprojection

CT attenuation map

SPECT
OSEM with attenuation, scatter, detector response compensation

Quantitative evaluation

Analysis method

Point source with known activity

SPECT

Sum all pixel intensity

Calibration factor (intensity/μCi)

Linear estimate

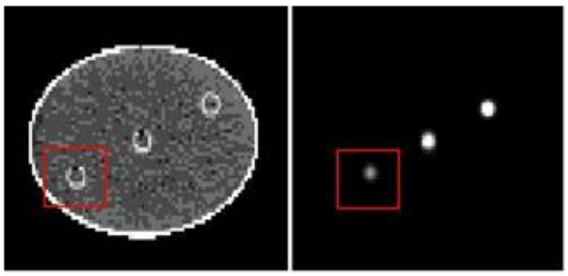

CT attenuation map

SPECT

VOI summed intensity/**μCi**

compare

Error

Define VOI on CT → Sum all pixel intensity in VOI on SPECT

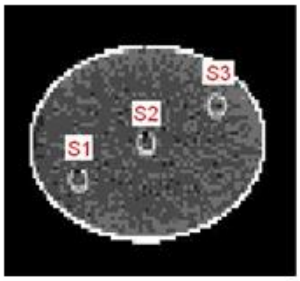

Quantitative analysis on experiment investigating concentration effect

VOI	S1	S2	S3
Radioactivity (mCi)	4.01	2.41	0.982
Reconstruction methods	% error		
FBP	-76.8	-89.7	-81.7
OSEM (all with 100 update)			
OSEM – without correction	-75.5	-89.3	-80.2
OSEM – CDR correction	-71.7	-86.7	-75.8
OSEM – attenuation correction	-3.37	-14.9	-12.0
OSEM – attenuation + CDR	9.67	5.97	7.13
OSEM – atten. + scatter + CDR	-0.645	-4.58	-2.93

TITLE:

Patient dose measurements during cardiac CT Angiography procedures.

AUTHORS:
Mahadevappa Mahesh, PhD

PURPOSE:

CT angiography is been increasingly performed in clinics these days. This has become possible due to recent advances in MDCT technology such as higher temporal and spatial resolution. However, the radiation doses in these procedures are also high.

Radiation dose and risk assessments for CT protocols are estimated based on the CTDI values measured using standard size and circular shaped phantoms. The actual doses to patients can vary widely due to their size, positioning and several other factors. The purpose of this project was to measure the radiation dose to patients undergoing CT angiography procedures directly by using thermoluminiscent dosimeters and to compare it with the values provided by the phantom measurements. The preliminary results on this project will be discussed in this talk.

METHODS AND MATERIALS:

RESULTS:

CONCLUSIONS:

TITLE: Theoretical Implications and Design Principles of Focused Multi-Pinhole SPECT

AUTHORS: Yuchuan Wang, Greta S.P. Mok, Benjamin M.W. Tsui

PURPOSE: We study, in theory, the advantages and implementations of focused multi-pinhole (FMPH) SPECT, in which, all of the pinhole apertures are tilted towards a common rodent-sized field-of-view (FOV) for maximum gain in detection efficiency.

METHODS AND MATERIALS: First, we establish two equations using system design parameters: one describes the photon detection efficiency (PDE), the other describes how well the Tuy's condition is satisfied within the FOV (defined as TSE: tomographic sampling efficiency). Among "resolution-equivalent" system designs with minimal projection-overlap, we show that the number of unknowns in the PDE equation is reduced to two: the number of pinholes (N) and the system radius-of-rotation (R) while maintaining a non-truncated FOV.

Next, we analyze that an optimal FMPH SPECT system should have high values of PDE and TSE. Therefore, designing such an imaging system becomes a process of finding system parameters that maximize PDE, and then TSE. Parameters N and R are directly obtained from PDE maximization, while aperture diameter (D) and collimator length (F) are calculated based on them. We then analyze the factors that affect TSE, including the number/placement of the pinholes and the total number of angular views. This analysis guides the placement of N pinholes, which completes the design process.

Implications of PDE and TSE maximization are shown by comparing FMPH SPECT and single pinhole (SPH) SPECT.

RESULTS: For a typical rodent imaging configuration of 26mm FOV and 25mm minimum R, to achieve a target resolution of 1.2mm, PDE maximization for a clinical SPECT camera (40cm detector size, 3.5mm intrinsic resolution) resulted in N=8, R=25mm, D=0.8mm, F=12 cm, and 4 times PDE over a resolution-equivalent optimal SPH design. For a modular camera (12cm detector, 1.5mm intrinsic), we obtain N=4, R=25mm, D=0.6mm, F=5cm, and 1.8 times PDE over the optimal SPH design.

To maximize TSE, we found that one should minimize the use of collinear sub-patterns, especially those parallel or perpendicular to the scanning orbit. Together with the consideration of minimizing projection overlap, we obtained two practical pinhole patterns for the above two cases, which have a TSE gain of 90% and 58% over SPH designs, respectively.

Simulation and experiment studies using the proposed FMPH SPECT designs demonstrated superior reconstructed image quality throughout the entire FOV as compared to the corresponding SPH SPECT. The benefit may also be traded for significantly reduced acquisition time without sacrificing reconstructed image quality.

CONCLUSIONS: FMPH SPECT may be a superior imaging method as compared to SPH SPECT in practical rodent imaging studies. We developed effective means of optimizing the FMPH design based on maximizing both photon detection efficiency and tomographic sampling efficiency.

FUNDING SOURCES: NIH R01 EB 001558

TITLE: **MicroComputed Tomography with a Photon-Counting X-Ray Detector**

AUTHORS:

E.C. Frey[1], K. Taguchi1, M. Kapusta[2], J. Xu[1], T. Orskaug[2], I. Ninive[2], D. Wagenaar[2], B. Patt[2], and B.M.W. Tsui[1]

[1]Russell H. Morgan Department of Radiology and Radiological Science, Johns Hopkins University, Baltimore, MD; 21287

[2]Gamma Medica-Ideas., Northridge, CA 91324

PURPOSE:

The goal of this work was to investigate the use of a novel CdTe photon counting x-ray detector (PCXD) capable of very high count rates to perform x-ray micro-computed tomography (microCT).

METHODS AND MATERIALS:

The detector had 2 rows of 384 square pixels each 1 mm in size. Charge signals from individual photons were integrated with a shaping time of ~60 ns and processed by an ASIC located in close proximity to the pixels. The ASIC had 5 energy thresholds with associated independent counters for each pixel. Due to the thresholding, it is possible to eliminate dark-current contributions to image noise. By subtracting counter outputs from adjacent thresholds, it is possible to obtain the number of x-ray photon counts in 5 adjacent energy windows. The detector is capable of readout times faster than 5 ms. A prototype bench-top specimen μCT scanner was assembled having distances from the tube to the object and detector of 11 cm and 82 cm, respectively. We used a conventional x-ray source to produce 80 kVp x-ray beams with tube currents up to 400 μA resulting in count rates on the order of 600 kcps per pixel at the detector. Both phantoms and a dead mouse were imaged using acquisition times of 1.8 s per view at 1° steps around the object. The count rate loss (CRL) characteristics of the detector were measured by varying the tube current and corrected for using a paralyzable model. Images were reconstructed using analytical fan-beam reconstruction. A water-phantom-based uniformity correction was used to reduce ring articats. A first generation CT geometry was also investigated by translating the object through the x-ray beam at each projection view and using the data for a single pixel to perform a parallel-beam reconstruction.

RESULTS:

Correcting for count rate losses was effective in restoring the linearity of the detected photons as a function of energy. However, for high energy windows, count rate increase with increasing tube current due to pulse pileup of low energy photons. The reconstructed images showed good contrast and noise characteristics and those obtained from different energy windows demonstrated energy-dependent contrast, thus potentially allowing for material decomposition. Anomolously high attenuation coefficients were observed in images reconstructed from photons in higher energy windows. This is also explainable by pileup of low energy photons in the high energy window. Significant rings were observed in reconstructed images. Deadtime correction resulted in a small reduction in rings. Imaging at a lower current (100 μA) did not result in a reduction in rings. The water phantom correction resulted in significant ring reduction. Heavily filtering the incident beam so that there were few photons below the lowest energy threshold resulted in significant ring reduction. Using a first-generation geometry resulted in ring-free images. These observations suggest that the source of the rings was pixel-to-pixel variations in spectral sensitivity, perhaps due to variations in energy response of the detectors or energy thresholds.

CONCLUSIONS:

This work has demonstrated the PCXDs have the potential to handle the count rates needed for microCT. The energy discrimination capability can be used for material composition or to provide improved visualization of materials through the use of optimal weighting of images obtained in the different energy windows. While count-rate losses do occur, compensation for these seems effective. Pulse pileup remains an issue and needs to be taken into account both in material composition analysis and in determining optimal weights. Rings artifacts are a serious limitation suggesting the need for improved pixel spectral uniformity, improved tuning of energy thresholds, and development of ring-compensation methods.

TITLE:

Investigation of the use of Photon Counting X-Ray Detectors with Energy Discrimination Capability for Material Decomposition in Micro-Computed Tomography

AUTHORS:

E.C. Frey, X. Wang, Y. Du, K. Taguchi, J. Xu, and B.M.W. Tsui

Russell H. Morgan Department of Radiology and Radiological Science, Johns Hopkins University, Baltimore, MD, 21287

PURPOSE:

Recently developed solid-state detectors combined with high-speed ASICs that allow individual pixel pulse processing may prove useful as detectors for small animal micro-computed tomography. One appealing feature of these photon-counting x-ray detectors (PCXDs) is their ability to discriminate between photons with different energies and count them in a small number (2-5) of energy windows. The data in these energy windows may be thought of as arising from multiple simultaneous x-ray beams with individual energy spectra, and could thus potentially be used to perform material composition analysis. The goal of this paper was to investigate the potential advantages of PCXDs with multiple energy window counting capability as compared to traditional integrating detectors combined with acquisition of images using x-ray beams with 2 different kVps.

METHODS AND MATERIALS:

For the PCXDs, we investigated 3 potential sources of crosstalk: scatter in the object and detector, limited energy resolution, and pulse pile-up. We used Monte Carlo simulations to investigate the importance of scatter in the object and the detector in producing crosstalk between projections in the different energy windows. We compared the precision and accuracy of basis decomposition for a PCXD with 2 or 5 energy windows using a single 80 kVp beam to either a single-energy-window PCXD, or an intensity integrating detector using a dual kVp method with 50 and 80 kVp x-ray beams. This comparison was performed using an analytic simulation and various thicknesses of Al and PMMA with a total PMMA-equivalent thickness of 3.0 cm. Measured energy spectra were used as the input to this simulation. To study the effects of energy resolution, we blurred the energy spectrum of detected photons with Gaussian functions having FWHMs of 1, 2, 5, and 10 keV. Basis decomposition was performed using a nonlinear parameter estimation method to estimate the thicknesses of the two basis materials. The method was calibrated using noise-free simulated data from 169 combinations of PMMA and Al thicknesses. The precision and accuracy was evaluated for a set 16 combinations of PMMA and Al thickness. For each combination we used 50 noise realizations. Bootstrap methods were used to estimate the standard deviations of the precision and accuracy measures. To study the effects of pulse-pileup we developed an analytic pileup simulation and modeled realistic resolving times and photon fluences.

RESULTS:

The Monte Carlo simulations showed that scatter in the object and detector resulted in relatively little crosstalk between the data in the various energy windows. The precision of estimating the thickness of two basis materials for a range of material compositions was slightly better for the single kVp multiple energy window acquisition methods compared to the dual kVp methods with an integrating detector. The precision of the estimates, as measured by the standard deviation averaged over all the thickness combinations investigated, was substantially better for the single kVp multi-energy-window methods. The advantage of the multi-window acquisition was somewhat reduced when the energy resolution was degraded to 10 keV and when pulse pileup was included., but remained better by more than a factor of 2. The 5-bin detector did not provide substantially better precision or accuracy than the 2-bin detector.

CONCLUSIONS:

Photon-counting x-ray detectors with energy discrimination capabilities have the potential to provide improved material basis decomposition. Scatter in the object or detector was not found to be a major factor for the microCT geometry and object investigated. Pulse pile-up and finite energy resolution in the PCXD resulted in poorer precision in the basis material thickness estimates, but the estimates remained substantially more precise than for conventional dual kVp methods.

TITLE:
The Quantitative Measurement of Iodine Concentration with Abdominal C-arm CT: Phantom Study

AUTHORS: Yoshinori Funama, PhD, David Graff, PhD, Jean-Francois H. Geschwind, MD, Elliot K. Fishman, MD, and Katsuyuki Taguchi, PhD

PURPOSE:
Many interventional radiological (IVR) procedures involve iodine contrast solution for planning, targeting, treatment, and evaluation. Measurement of the iodine distribution will lead us to quantitative, evidence-based IVR procedures. Our aim was to develop methods to quantify the iodine concentration for abdominal IVR procedures using phantom studies.

METHODS AND MATERIALS:
A C-arm CT scanner with a 19" flat-panel detector (Allura Xper FD20; Philips Medical Systems, Best, The Netherlands) and a 64-slice CT scanner (Sensation 64; Siemens Medical Solution, Erlangen, Germany) were used. As the limited detector size cannot image the entire abdomen, the resulting "truncation" artifact is inevitable in C-arm CT images for abdominal applications. Thus, we evaluated the following two aspects using an elliptic-cylindrical water bath phantom with inserts filled with iodine-water solution: (1) the effect of the truncated field-of-view by shifting the phantom (27-142 mm outside of the detector coverage) to simulate slim to very obese patients; and (2) the accuracy of iodine concentration with various mixture ratio (2.32-31.82 mgI/mL). In both settings, pixel values of C-arm CT images were converted to Hounsfield unit-like (HU_CCT) values by using the ratio of the pixel value with enhancement and the background. The iodine concentration was then calculated from the converted HU_CCT value using x-ray mass attenuation coefficient and mass density of iodine and water.

RESULTS:
From 27 mm to 142 mm of the truncation, the pixel values of C-arm CT images varied as much as 53%. However, the converted HU_CCT values varied less than 5%. With various iodine concentration (55-626 H.U. in CT images), the converted HU_CCT value of C-arm CT and pixel values of CT images showed very strong correlation (r2 = 0.99). The root-mean-squared errors of the estimated iodine concentration (see figure) were 0.11 mgI/mL (-13 % to +9% error) with C-arm CT and 0.07 mgI/mL (-6% to +9% error) with CT, respectively.

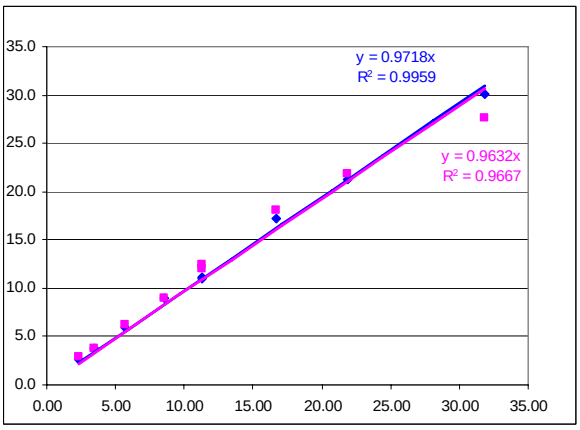

CONCLUSIONS:
The effect of truncation in abdominal procedures can be reduced from 53% to 5% by converting pixel values to the Hounsfield unit-like values (HU_CCT) using the proposed method. With the method, the iodine concentration can be quantitatively measured with an error of -13 % to +9 %.

FUNDING SOURCES:
Philips Medical Systems

TITLE: Soft tissue imaging in transcatheter arterial chemoembolization: Image quality and potential utilities

AUTHORS: D. S. Graff, K. Taguchi, C. Georgiades, E. Liapi, K. Hong, J.H. Geschwind

PURPOSE:
To objectively measure the ability of Soft tissue imaging C-arm computed tomography (STICA-CT) combined with a diagnostic MRI to predict, monitor, and evaluate the tumor coverage and risk of complications of a TACE treatment.

METHODS AND MATERIALS:
We perform two complementary studies: a reading study establishes the objective ability of STICA-CT images to measure quantities useful for TACE, and then describe two cases in which STICA-CT is used to aid in TACE. *Part 1*: Twenty-five TACE procedures were performed in nineteen patients (12 men, 7 women; mean ± std. dev. age, 59 ± 10 years). In all cases, gadolinium contrast-enhanced MRI scans were performed prior to the TACE procedure, STICA-CT scans were performed during the TACE procedure and standard CT scans were performed the next day. Three types of STICA-CT scans were (1) pre-treatment with iodine contrast (n = 3); (2) mid-treatment with contrast (n = 3); and (3) post-treatment without contrast (n = 25), respectively. Two independent interventional radiologists who did not participate in the treatment of the patients assessed the various images to estimate the location, size, shape, and degree of enhancement of tumors, classify the pattern of enhancement of tumors, and establish the presence and degree of enhancement in normal tissue outside tumors. *Part 2*: Two TACE procedures are detailed to illustrate the implementation of STICA-CT in TACE.

RESULTS:
Part 1: All tumors (n = 33) larger than 1.8 cm and 10 out of 17 smaller tumors were identified in STICA-CT scans at the same locations as in MRI scans. A comparison of the post-treatment STICA-CT with CT showed that STICA_CT is able to measure the sizes of enhanced tumors with a standard deviation of 20%, comparable to the s tandard deviation and underestimates the size of some tumors with lightly enhanced shells due to insufficient low-contrast resolution. STICA-CT can be used to measure the shape of the enhanced region, and can measure the percent of the tumor that is treated with a standard deviation of 26% and a bias of -15% ± 4%. The enhancement pattern of tumors in post-treatment STICA-CT images agreed with that determined by CT in 79% ± 1% of tumors. Contrast enhanced STICA-CT scans were able to predict the corresponding measurement post-TACE CT: the size of the treated region with a standard deviation for a single tumor of 37%; the degree of enhancement with a standard deviation for a single tumor of 30%; and the pattern of enhancement in 50% of tumors. Mid-treatment scans underestimated the final size of the treated region by 27 ± 11%. The presence of enhancement outside tumors could be measured with STICA-CT with a sensitivity of 76–95% and a specificity of 53–95% (95% confidence). The size, shape, degree and pattern of enhancement of tumors could be compared with a pre-treatment diagnostic MRI with similar accuracy and precision. *Part 2*: In one described patient, contrast-enhanced and mid-treatment STICA-CT scans revealed that a targeted tumor mass was not treated. The resulting modifications in catheter position led to a more complete coverage of tumor. In another described patient, contrast-enhanced STICA-CT scans showed a risk of dangerous deposition of chemo-embolizing treatment to the stomach. The resulting change in the injection intensity avoided a potential major complication.

CONCLUSIONS:
Our data suggest that even under unfavorable abdominal conditions, STICA-CT scans faithfully record the features of images used to assess the success and risk of complications of a TACE treatment: the location, size, shape, degree, and pattern of deposition of the chemo-embolizing mixture and its deposition outside of tumors. These features can be compared to pre-treatment MRI scans of patients to measure to what extent the appropriate tumors are being treated. Our preliminary data showed that a pre-treatment contrast scan can be used to predict the success of a proposed treatment, and the risk of complications, and that a minority of patients with difficult anatomy could thereby enjoy improved treatment.

FUNDING SOURCES:
Philips Medical Systems

TITLE:
Optimization of a 3D cardiac motion estimation method using simulated gated SPECT images

AUTHORS:
Jing Tang, W. Paul Segars, Taek-Soo Lee, Xin He, and Benjamin M. W. Tsui

PURPOSE:
The goal of this study is to optimize the performance of a 3D cardiac motion estimation method for gated myocardial perfusion SPECT images in the task of distinguishing between hearts with and without regional motion defect.

METHODS AND MATERIALS:
Simulated noise-free gated myocardial perfusion SPECT projection data with 16 frames were generated from two 4D NCAT beating heart phantoms, one with normal motion and the other with a 50% motion defect in a pie-shaped region-of-interest (ROI) on the left ventricle (LV). Poisson noise fluctuations were added to the clinical-count-level scaled noise-free projection data to generate 40 realizations of noisy projection datasets. A 4D MAP-RBI-EM algorithm with corrections of attenuation, collimator-detector response, and scatter was used in the image reconstruction. Two gated frames, one at the end-diastole and the other in the middle of the cardiac expansion, where the radial motion is the largest, were used for optimizing the performance of the motion estimation method in distinguishing between normal and abnormal beating hearts. The signal-to-noise ratio of the radial motion over the ROI was determined from the difference between its averages of the normal and the abnormal beating hearts and its variations in all the noise realizations. The AUC value for each individual frame is calculated from its signal-to-noise ratio. The performance of the motion estimation method is optimized through choosing the myocardial strain energy weighting factor (β) in its cost function that maximizes the AUC value.

RESULTS:
In the range β was tested, the AUC value peaked at $\beta = 0.005$ for both the selected frames. The peak AUC values are 0.88 at the end-diastole frame and 0.91 at the middle expansion frame, respectively.

CONCLUSIONS:
The choice of the myocardial strain energy weighting factor (β) affects the performance of the motion estimation method in distinguishing between hearts with and without regional motion defect. The hence optimized β matches well with that previously obtained from minimizing the root-mean-square error of the end-diastole LV motion vector field (MVF) estimated from ideal normal images with respect to the built-in MVF.

FUNDING SOURCES:
NIH R01 EB 000168 & R01 HL068075

TITLE:

Direct iterative reconstruction of regions-of-interest activities for SPECT imaging

AUTHORS:

Y. Du, E.C. Frey, and B.M.W. Tsui

PURPOSE:

We have developed an OS-ROI algorithm to allow direct estimation of activities in uniform regions-of-interest (ROIs) with intrinsic compensation for partial volume effects.
The method supports the use of ROI sets that do not completely fill the object and updates voxels outside the ROIs as in conventional OS-EM. The OS-ROI provides higher quantitative accuracy and precision than OS-EM with post reconstruction partial volume compensation (PVC) but suffers low convergence when ROI sets do not contain whole object. In this work, we improved the OS-ROI by adding Gibbs prior when updating voxels outside the ROI sets.

METHODS AND MATERIALS:

In this work, we improved the OS-ROI by adding Gibbs prior when updating voxels outside the ROI sets. The method, referred to as OS-ROI-MAP, was evaluated using Monte Carlo simulated projections of brain phantoms containing uniform striatal components and backgrounds. Data were reconstructed using OS-EM or OS-ROI and OS-ROI-MAP with two different ROI sets that included only the striatum or both the striatum and background.

RESULTS:

Quantitative results showed that when ROI set contain whole object, OS-ROI-MAP performed identically as OS-ROI and both gave less bias and higher precision than OS-EM with PVC. When ROI set only contain the striatum, the striatal activity estimates from OS-ROI were still not converging after 30 iterations. The results from OS-ROI-MAP, however, converged much faster. At 30 iterations, the accuracy and precision were higher than PVC and OS-ROI. The results were close to those of OS-ROI with the ROI set contained whole brain.

CONCLUSIONS:

In conclusion, the OS-ROI-MAP method improves convergence and provides better accuracy and precision compared to the original method.

FUNDING SOURCES:

Funded by the Public Health Service Grant R01 CA 109234 and NIBIB Grant R01 EB000288